Fuel 407 (2026) 137294

Contents lists available at ScienceDirect

Fuel

journal homepage: www.elsevier.com/locate/fuel

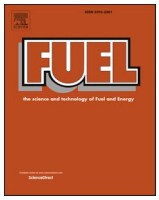

Full Length Article

An Automated, geometrically faithful pore network model for diffusion and reaction in biomass char

Thomas Sheehan [a], Marek Trawicki [b], Simcha Singer [a,*]

[a] Department of Mechanical Engineering, Marquette University, Milwaukee, WI 53233, USA
[b] Department of Mathematical and Statistical Sciences, Marquette University, Milwaukee, WI 53233, USA

ARTICLE INFO

Keywords:
Biomass
Combustion
Pore Network Model
Graph
X-ray Micro-Computed Tomography

ABSTRACT

Biomass char particles are often morphologically complex and contain large pores in addition to sub-micron porosity. The complex morphology impacts overall reaction rates for zone II conditions, which affects reactor-scale behavior. Computational fluid dynamics (CFD) simulations for reactors therefore require particle models that are computationally efficient, yet able to account for real biomass morphologies. While generalized effectiveness factor models can represent reaction and diffusion within irregularly shaped microporous solid regions, these upscaled models are not valid for large pores. To that end, a geometrically faithful pore network model has been developed to model diffusion and reaction in biomass char pores, using automated image processing and graph construction based on X-ray micro-computed tomography (micro-CT). Because biomass pores are often long and straight, 1-D pores are employed, with lengths, surface areas, and volumes obtained from micro-CT. Different solutions for internal, dead-end, and surface pores are then implemented. By balancing molar fluxes into each node, the reactant mole fraction throughout the network and the average mole fraction on the pore-solid interface, which is required by generalized effectiveness factor models, are determined. The model is validated by comparing morphological properties of the 1-D pore network to those obtained from 3-D imaging and by comparing mole fraction predictions to those from 3-D, geometrically faithful, pore-resolving CFD. The model reproduces features from CFD, including regions of relatively high and low reactant mole fraction, capturing the impacts of pore connections and external openings, and achieved <10% average relative error in reactant mole fraction without using fitting parameters.

1. Introduction

Biomass char particles are often morphologically complex and contain relatively large pores [1] interspersed in a "microporous solid" matrix composed primarily of carbon, mineral matter, and smaller pores (micropores, mesopores, and macropores). While the morphology of biomass char depends on the fuel's lignocellulosic composition [2] and devolatilization conditions [3,4], large pores with high aspect ratios, cellular structures, and a significant degree of directional porosity are often observed [2,5,6].

Char morphology impacts particle-scale combustion and gasification rates under zone II conditions [7–9], in which diffusion and reaction both influence overall rates. This, in turn, can impact reactor-scale behavior for biomass particles [10,11]. Reactor-scale computational fluid dynamics (CFD) simulations therefore require particle-scale models that are computationally efficient, yet able to account for real distributions of biomass morphology.

Because biomass char particles contain pores over a wide range of length scales [3] with considerable morphological complexity, it is impossible to solve conservation equations for transport and reaction throughout the entire pore space. Instead, conservation equations in models for combustion or gasification of porous particles are usually upscaled using homogenization [12] or volume averaging [13]. These "effective continuum" models solve conservation equations for a composite medium comprised of unresolved, subgrid-scale pores and solid, with effective coefficients which, in theory, depend on the morphology [14]. However, to be valid and accurate, upscaling requires a separation of length scales [14]; the characteristic length of the pores must be significantly smaller than the particle as well as the characteristic length of the physical processes to be resolved (e.g., species gradients). Many biomass char particles contain pores that are sufficiently large [1,2,4] that they cannot be treated at the subgrid-scale for sub-millimeter

* Corresponding author.
E-mail address: simcha.singer@marquette.edu (S. Singer).

https://doi.org/10.1016/j.fuel.2025.137294
Received 22 July 2025; Received in revised form 12 September 2025; Accepted 21 October 2025
Available online 4 November 2025

biomass particles.

To address the lack of scale separation, some researchers have performed 3-D pore resolving simulations using idealized particle geometries (e.g., [15]), using procedurally generated particles based on 3-D imaging [5,16], or using real particle geometries obtained from 3-D imaging, which is the highest fidelity approach [11]. In the latter, geometrically faithful approach, real char particles were imaged in three dimensions using X-ray micro-computed tomography (micro-CT), [9,17,18] with pores larger than a couple microns being resolved [9,18]. Geometrically faithful CFD simulations were then performed, with conservation equations based on first principles solved in the resolved pores which are not amenable to upscaling, and effective continuum equations solved only in the microporous solid regions. It was found that large pores act as conduits for diffusion of oxygen throughout the particles, with enhanced penetration to the innermost regions [9,18]. An equivalent spatially resolved effective continuum model with all porosity modeled at the subgrid-scale was unable to reproduce the impact of the larger pores on long range transport [9].

Micro-CT-based, geometrically faithful, non-reactive CFD has been employed to study the impact of porous coal char morphology on heat transfer, fluid flow, and drag [19,20] and to study the impact of biomass and biochar pore structure on anisotropic permeabilities [21,22]. The anisotropy in permeabilities decreased for the post-pyrolysis biochar compared to the original biomass for both hardwood and softwood, due to the development of pores perpendicular to the main pore directions [21].

While useful for studying the fundamental impact of biomass morphology on reaction and transport, the computational expense of 3-D geometrically faithful CFD makes it prohibitive for particle-scale modeling within reactor-scale simulations. Classical effectiveness factor models, which are based on exact or approximate solutions to upscaled reaction–diffusion equations in porous particles, are computationally efficient and appropriate for reactor-scale CFD but cannot accurately account for the impact of large pore morphology for zone II conditions. While effectiveness factor models have been developed for 1-D or 2-D hollow cylinders and spheres [23] to account for a single, central, resolved large pore, the geometrical simplicity may be too restrictive for many real biomass chars.

Another class of effectiveness factor models, descended from the work Aris [24], can account for the impact of irregular three-dimensional geometries using 1-D models. These generalized 1-D models [25] employ the particle's volume-to-surface-area ratio as a characteristic length and make use of asymptotic solutions to the reaction–diffusion equation at low and/or high Thiele modulus [26–29]. Recent versions, such as the one-dimensional generalized cylinder (1D-GC) models, have shown excellent agreement with 3-D CFD for real, complex catalyst geometries [29]. However, being upscaled models, these generalized effectiveness factor models can only account for diffusion and reaction in microporous solid regions with purely subgrid-scale porosity. Therefore, to predict the overall reaction rate in biomass char using a generalized 1-D effectiveness factor model, the average [30] reactant concentration on the interface between the microporous solid and the large pores (and external surface) must be known. While this interfacial concentration is often readily known in catalysis applications [29,31], since minimal concentration gradients exist outside the microporous solid, for high temperature combustion and gasification, concentration gradients in the large pores (and outside the particles) are often significant and are not readily calculated for complex pore geometries [18]. Therefore, even when using a generalized 1-D effectiveness factor model suitable for irregular solid geometries, an impediment to determining the overall reaction rate is an accurate prediction of the reactant concentration on the interface between the large pores and the microporous solid.

This paper's objective is therefore to develop a computationally efficient, accurate, automated, and geometrically faithful pore network model for diffusion and reaction in the pore space of real biomass char particles, using real 3-D particle geometries obtained from high-resolution micro-CT imaging. Biomass may be particularly suited to pore network modeling, given the often 1-D nature of its large pores [6]. This meso-scale pore-space model for biomass char particles predicts the local and average reactant concentration at the interface between the large pores and the microporous solid and requires just a few seconds of runtime, after automated pre-processing to construct the pore network, compared with the dozens of hours required for pore-resolving CFD. The geometrically faithful pore network model can be paired with an existing generalized 1-D effectiveness factor model for reaction and diffusion in the irregularly shaped microporous solid to obtain predictions of the overall reaction rate for realistic biomass char particles.

While pore network models for solving systems of reaction–diffusion equations have been developed for several applications and at scales from particles to reactors [32–34], the first novelty of this work is that it constitutes the first application of a pore network reaction–diffusion model to biomass. Indeed, while 3-D imaging has been used to construct pore networks for biomass [35], biochar [36], and to analyze the network properties' dependence on feedstock and evolution with pyrolysis conditions, those pore networks were not employed to solve systems of equations for transport and reaction, or to determine concentration distributions throughout the particles.

Furthermore, to the authors' knowledge, this paper also represents the first geometrically faithful, reaction–diffusion pore network model for thermochemical porous particles of any type (i.e., milled/ground coal or biomass, catalysts, or oxygen carriers), which constitutes the second novelty of this paper. While pore network models have been used to solve for reaction and diffusion in catalyst particles, those pore networks have been based on synthetically generated geometries, whether structured [37–41] or unstructured (e.g., randomly positioned spheres [42]). Beyond thermochemical processes, pore-resolving simulations [43] and pore network reaction–diffusion models have been employed to study geochemical processes in rock [44], including studies that have derived the pore networks from real geometries obtained from micro-CT [45,46].

Finally, unlike previous particle-scale pore network reaction–diffusion models, the present model is directly validated using 3-D geometrically faithful pore-resolving CFD simulations for the same geometries, without the use of any fitting parameters. In contrast, previous models using synthetically generated pore networks did not validate the model (e.g., [37,41]), matched analytical solutions for simple 1-D geometries [39], or employed fitting parameters to match analytical solutions for simple geometries [42]. An exception is the work of Huang et al., [40], which performed validation for a more complex geometry, but using 2-D CFD.

The automated, geometrically faithful pore network model developed in this paper comprises a portion of a workflow being developed to capture the impacts of real biomass char morphology for distributions of particles in reactor-scale CFD codes. The workflow requires micro-CT imaging of a representative particle distribution, followed by automated 3-D image processing to measure key morphological parameters for each biomass char particle in the distribution. The representative distribution of biomass particles, with its concomitant distribution of sizes and morphologies obtained in the pre-processing step, can then be used to inform computationally efficient and accurate particle-scale models for a distribution of particles to be used in reactor-scale CFD. The particle scale models would be comprised of the pore network model developed here for the large pore space, paired with a generalized 1-D effectiveness factor model for the microporous solid.

2. Methods and models

This section describes the micro-CT imaging, as well as the image processing, segmentation, and measurement of the morphological properties of the resolved pore space. It then describes the automated construction of the graph that represents the resolved pore space, explains the different types of edges and nodes comprising the graph, and

outlines the procedure to determine the length, cross-sectional area, and perimeter of each pore (edge) in the network. The pore network reaction–diffusion model is then presented in detail, describing the equations used for each type of pore and the matrix equations used to solve for the reactant concentration at all nodes and within each pore in the network. This section also contains an overview of the geometrically faithful, pore-resolving CFD simulations, which have been described in detail elsewhere [17,18] and which are used to validate the pore network model and explains how parameters used in the pore network model have been chosen to be consistent with the CFD.

2.1. Materials and micro-CT maging

Poplar chips (¼ inch) were obtained from the Bioenergy Feedstock Library at Idaho National Laboratory. Poplar is a hardwood species that has been studied using 3-D imaging and simulation [5,11,16,47]. The woody biomass was 0.87% ash and 12.65% fixed carbon on a dry, ash-free basis. The biomass was torrefied in argon at 280 °C to increase grindability. It was ground with a mortar and pestle and sieved to 250 μm. The sample was then devolatilized at 1073 K for 60 s to produce char. Dozens of biomass char particles were mixed with < 200 μm glass bubbles, which served to support and disperse the biomass char during micro-CT imaging. The mixture was placed in a micropipette tip and imaged using micro-CT (GE v|tome|x s 240) at 60 kV and 190 μA with a voxel size of 1.55 μm.

2.2. Image processing, segmentation, and morphology characterization

The stack of TIFF files from micro-CT reconstruction was processed using a MATLAB workflow which first extracted individual biomass char particles into separate image stacks. Particles were separated from each other and from the support material using watershed segmentation. Pieces of support material that remained in the cropped image were removed using several automated techniques, including a brightness filter, a filter based on the sphericity of the support material, and an erosion operation. Separated biomass char particles were then segmented into microporous solid regions and resolved pores using thresholding. The pore space of the biomass char particle was created using binary subtraction of the 3-D solid from a version of the 3-D particle that had undergone a closing operation. The 3-D pore model was filtered using an area opening filter to remove noise. Fig. 1 shows the segmented geometries for three particles chosen at random and used in this study, termed particles P1, P2, and P3. The particles are highly anisotropic, as previously observed for poplar (and other biomass feedstocks) via 3-D imaging [47], and each particle has several irregular protrusions. The particles exhibit anisotropic surface roughness and ridges similar to those previously observed for poplar using micro-CT imaging [47]. The surface renderings of the segmented particles in Fig. 1 also reveal frequent pore openings along the surface of the anisotropic particles.

Basic morphological properties of the 3-D solid and its pore space, including total particle volume, pore volume, and pore surface area, were calculated using image analysis tools in MATLAB. To determine the locations of the pore openings on the external surface, which are needed in the pore network model, the 3-D pore space was slightly dilated, and its overlap with the external surface yielded the locations of pore openings on the external surface.

2.3. Automated graph generation and characterization

The first step in converting the 3-D pore space to a graph representation with edges representing the pores, and nodes representing pore intersections with each other, with the external surface, or dead ends, is skeletonization (medial axis thinning) of the pore space [48]. The skeletonized pore space is then converted to a graph using an automated workflow that turns each voxel in the skeleton into a node, with adjacent nodes being connected by edges. The skeleton-to-graph conversion was adapted from the MATLAB script in [49]. The graph arbitrarily assigns a "source" and "target" node to each edge.

Redundant nodes and edges are then removed, such that each of the graph's edges represents distinct pores, and the graph's nodes represent intersections between pores, as well as external surface openings and dead ends. Thus, any internal nodes that are connected to only two other internal nodes are removed (since these three nodes represent a single pore) and the two remaining nodes are subsequently connected by a single edge. To preserve the external pore openings and their locations, nodes that are marked as being external are restricted from removal operations, as are their adjacent internal nodes. In addition, branching locations may initially be represented as clumps of nodes, instead of a single node with more than two connecting edges. In such a case, the clump of nodes is reduced to a single node while maintaining all connecting edges that are external to the clump.

Since the reaction–diffusion equation's boundary conditions and solution will vary depending on the location and connectivity of the pores, the nodes and edges in the graph are classified accordingly. With reference to the schematic graph in Fig. 2, regular edges and nodes occur on the interior of the graph and are shown in blue. Surface nodes occur on the particle's external surface and are shown in green. A single far-field boundary node across the boundary layer from the particle is added to the graph and shown in magenta in Fig. 2. Boundary layer edges are placed between surface nodes and the far-field boundary node and are shown in green. Dead-end nodes are nodes connected to just a single edge (excluding the far-field boundary node, which could potentially be connected to a single edge) and are shown in red, while dead-adjacent nodes are adjacent to dead-end nodes and are shown in orange. Dead-end edges are the edges between dead-end nodes and dead-adjacent nodes, and are shown in red.

To utilize the graph in the pore network reaction–diffusion model, the length, average cross-sectional area, and average perimeter of each pore (edge) must be determined. The length of each pore is determined

Fig. 1. Segmented biomass char particles P1, P2, and P3 (left to right), with microporous solid shown in red and resolved pore openings on external surface visible in blue.

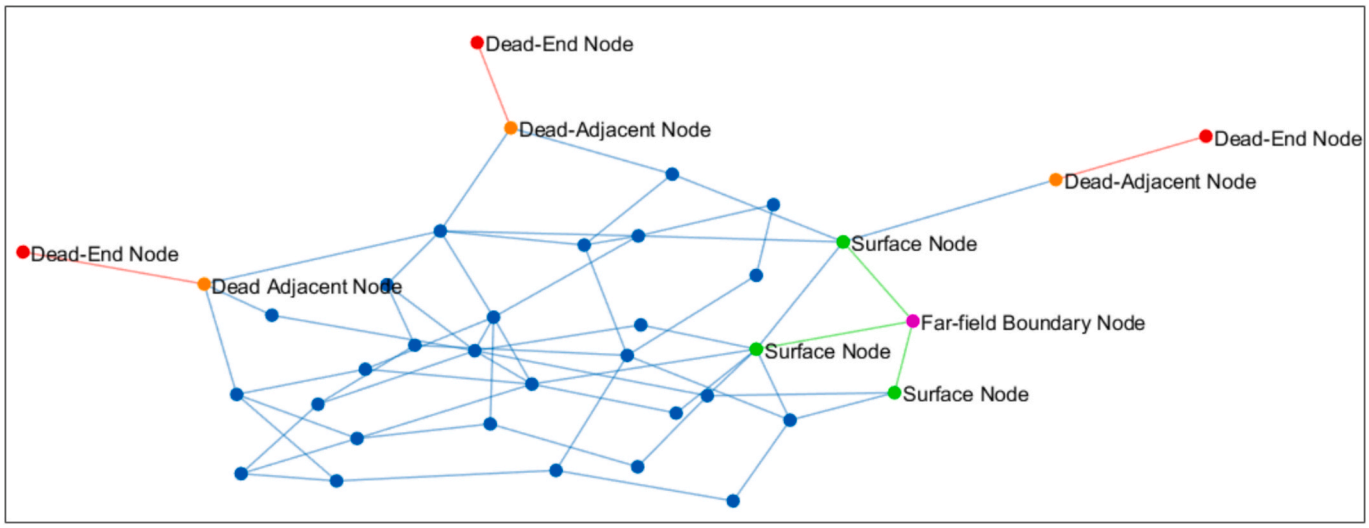

Fig. 2. Graph schematic illustrating five types of nodes: dead-end nodes, dead-adjacent nodes, internal nodes (unlabeled), surface nodes, and far-field boundary node.

by using the coordinates of its two nodes to calculate the distance between them. To determine the average cross-sectional area and perimeter of each pore, at each point along an edge, a sample plane perpendicular to the pore is overlayed on the 3-D pore space. The overlap between the sample plane and the 3-D pore space is used to calculate the pore's local cross-sectional area and perimeter at the location of that sample plane. The cross-sectional areas and perimeters are then averaged along the length of each individual pore. Since many pore sections, especially near branches in the pore space, overlap, voxels that have already been counted in a previous sample plane are omitted. An implication of this procedure is that the order in which the pore sections are analyzed could affect the average area and perimeter of the pores. Thus, a priority metric was employed to prioritize pores leading to external nodes, pores with higher network centrality, and finally, the degree to which the directionality of the pore aligned with the directionality of the particle, since it was noted that the largest, most important pores tended to be central to the pore network and directionally aligned with the particle axis. All calculations were performed in MATLAB.

2.4. Reaction-diffusion model on pore network

Because most large pores in biomass have high aspect ratios and are approximately one dimensional, analytical solutions for diffusion and heterogeneous reaction along 1-D pores are applied for every pore in the network, considering different solutions for internal pores, dead-end pores, and pores that intersect the external surface. The governing 1-D reaction–diffusion equation in the pore's axial direction at steady-state and in the case of a first order reaction on the pore's surface, is [50]:

$$\frac{d^2C}{dx^2} - \frac{P\ddot{k}}{DA}C = 0 \tag{1}$$

where C is the concentration of reactant, P is the perimeter of the pore's cross-section, $\ddot{k}$ is the heterogeneous reaction rate coefficient (m/s) on the pore's surface, D is the diffusion coefficient, and A is the pore's cross-sectional area. We define

$$\phi = \frac{P\ddot{k}}{DA} \tag{2}$$

and note that the pore Thiele modulus, Φ, is given by:

$$\Phi = \frac{L}{2}\sqrt{\phi} \tag{3}$$

where L is the pore length. Solving the governing equation between pore ends $x = 0$ (source) and $x = L$ (target), with Dirichlet boundary conditions of yet unknown concentrations C_B and C_L, respectively, for internal pores yields the concentration profile, $C(x)$, and the molar fluxes, J, in the positive x-direction at $x = 0$ (denoted J^-) and at $x = L$ (denoted J^+), in Eqs. 4(a)-4(c) in Table 1. For dead-end pores, either the node at $x = 0$ or $x = L$ has a Neumann boundary condition corresponding to zero flux. Whether the no-flux condition is applied at $x = 0$ (with condition $C = C_L$ at $x = L$) or at $x = L$ (with condition $C = C_B$ at $x = 0$) the concentration profiles and the fluxes at the "source" and "target" nodes can be obtained by analytical solution, as shown in Eqs. 5(a)-5(c) and Eqs. 6(a)-6(c) in Table 1.

The concentration profiles and molar fluxes depend on the node concentrations, C_B and C_L, which remain to be determined. For this purpose, a modified version of "Kirchoff's current law" is applied to all nodes in the network, since at steady state, the net flux into each node in the network is zero. Each pore, i, corresponds to an edge ($i = 1{:}e$) in the graph, while each pore end, which can be an intersection with another pore, a dead end, or an intersection with the external surface, corresponds to a node ($j = 1{:}n$) in the graph. However, in contrast to Kirchoff's current law for electrical resistor networks, in which every edge has a single current (flux) [51], in the present application each edge in the graph has two molar fluxes, with one defined at each end. This difference is due to heterogeneous reaction, which consumes reactant (oxygen) along each pore, resulting in molar fluxes that change with location along the pores.

Matrix operations are used to calculate the concentrations at each node. The graph's incidence matrix, $\bar{\bar{I}}$, has n rows corresponding to the nodes, e columns corresponding to the edges, and contains entries of −1 if node j is the source ($x = 0$) for edge i, entries of 1 if node j is the target ($x = L$) for edge i, and entries of 0 if a node j is not connected to edge i. The transpose of the incidence matrix is represented by the e x n matrix.

$$\bar{\bar{A}} = \bar{\bar{I}}^T \tag{7}$$

We define (using the element-by-element multiplication operation, $\circ$) the $2e$ x n matrix

$$\bar{\bar{A}}_{big} = \left[\bar{\bar{A}} \circ (\bar{\bar{A}} < 0)\; \bar{\bar{A}} \circ (\bar{\bar{A}} > 0)\right] \tag{8}$$

as well as its transpose, $\bar{\bar{A}}_{big}^T$, an n x $2e$ matrix, which will be used in Kirchoff's current law to account for "negative [sides of] edges" (with

Table 1
Concentration profiles and fluxes for regular and dead-end pores (edges).

Edge	Concentration Profile, $C(x)$	Flux J^- $(x = 0)$	Flux J^+ $(x = L)$	Eqs.
Internal	$\frac{C_B\sinh(\phi(L-x)) + C_L\sinh(\phi x)}{\sinh(\phi L)}$	$D\frac{C_B\phi\cosh(\phi L) - C_L\phi}{\sinh(\phi L)}$	$D\frac{C_B\phi - C_L\phi\cosh(\phi L)}{\sinh(\phi L)}$	4(a,b,c)
Dead-end (at $x = 0$)	$\frac{C_L\cosh(\phi x)}{\cosh(\phi L)}$	0	$-DC_L\phi\tanh(\phi L)$	5(a,b,c)
Dead-end (at $x = L$)	$\frac{C_B\cosh(\phi(x-L))}{\cosh(\phi L)}$	$DC_B\phi\tanh(\phi L)$	0	6(a,b,c)

fluxes J^-, adjacent to source nodes) and "positive [sides of] edges" (with fluxes J^+, adjacent to target nodes):

$$\overline{\overline{A}}_{big}^{T} = [\bar{\bar{I}}\circ(\bar{\bar{I}} < 0) \quad | \quad \bar{\bar{I}}\circ(\bar{\bar{I}} > 0)] \tag{9}$$

The rows of $\overline{\overline{A}}_{big}^{T}$ represent the n nodes, while columns 1:e contain entries of 0 or −1, with 0 representing no connection between an edge and node, and −1 representing "negative edges" i that intersect source nodes j. Similarly, columns $e + 1$:$2e$ of $\overline{\overline{A}}_{big}^{T}$ contain entries of 0 or 1, with the latter representing "positive edges" i that intersect target nodes j.

To implement Eqs. (4)-(6) in matrix form for the entire pore network, column vectors comprised of the molar fluxes at "negative edges" and "positive edges" (which depend on the vector of node concentrations, $\vec{C}$, to be determined) are given by

$$\overrightarrow{J^-} = -D\overline{\overline{\phi}}_{neg}\left(\overline{\overline{A}}\circ\overline{\overline{A}}_{neg}\right)\vec{C} \tag{10a}$$

$$\overrightarrow{J^+} = -D\overline{\overline{\phi}}_{pos}\left(\overline{\overline{A}}\circ\overline{\overline{A}}_{pos}\right)\vec{C} \tag{10b}$$

in which the e x n matrices $\overline{\overline{A}}_{neg}$ and $\overline{\overline{A}}_{pos}$ are defined by

$$\overline{\overline{A}}_{neg} = (\overline{\overline{A}} < 0)\circ\overline{\overline{A}}_{cosh} + (\overline{\overline{A}} \geq 0) \tag{11a}$$

$$\overline{\overline{A}}_{pos} = (\overline{\overline{A}} > 0)\circ\overline{\overline{A}}_{cosh} + (\overline{\overline{A}} \leq 0) \tag{11b}$$

the diagonal e x e matrices $\overline{\overline{\phi}}_{neg}$ and $\overline{\overline{\phi}}_{pos}$ are defined by

$$\overline{\overline{\phi}}_{neg} = diag(\phi_i/\sinh(\phi_i L_i)) \tag{12a}$$

$$\overline{\overline{\phi}}_{pos} = diag(\phi_i/\sinh(\phi_i L_i)) \tag{12b}$$

and the e x n matrix $\overline{\overline{A}}_{cosh}$ is defined by

$$\overline{\overline{A}}_{cosh} = \begin{bmatrix} \cosh(\phi_1 L_1) & \cdots & \cosh(\phi_1 L_1) \\ \vdots & \ddots & \vdots \\ \cosh(\phi_e L_e) & \cdots & \cosh(\phi_e L_e) \end{bmatrix} \tag{13}$$

Because dead-end edges have different expressions for $\overrightarrow{J^-}$ and $\overrightarrow{J^+}$ (see Table 1) the matrix equations (11a), (11b), (12a), and (12b) must be modified to yield the correct expressions when using Eqs. (10a) and (10b). If the dead-end occurs at the source ($x = 0$) node, j, for a given dead-end edge, i, the elements $\overline{\overline{A}}_{neg}(i,j)$ are set to zero for both the dead-end node and for its dead-adjacent node, to enforce Eq. (5b). Furthermore, to enforce Eq. (5c), the element $\overline{\overline{A}}_{pos}(i,j)$ is set to zero for the dead-end node, the element $\overline{\overline{A}}_{pos}(i,j)$ is set to one for the dead-adjacent node, and the element $\overline{\overline{\phi}}_{pos}(i,i)$ is changed to

$$\overline{\overline{\phi}}_{pos}(i,i) = \phi_i\tanh(\phi_i L_i). \tag{14}$$

Similarly, if the dead-end occurs at the target ($x = L$) node, j, for a given dead-end edge, i, the elements $\overline{\overline{A}}_{pos}(i,j)$ are set to zero for both the dead-end node and for its dead-adjacent node, to enforce Eq. (6c). Furthermore, to enforce Eq. (6b), the element $\overline{\overline{A}}_{neg}(i,j)$ is set to zero for the dead-end node, the element $\overline{\overline{A}}_{neg}(i,j)$ is set to one for the dead-adjacent node, and the element $\overline{\overline{\phi}}_{neg}(i,i)$ is changed to

$$\overline{\overline{\phi}}_{neg}(i,i) = \phi_i\tanh(\phi_i L_i). \tag{15}$$

Transport across an external boundary layer via boundary layer edges between the far-field boundary node and the surface nodes has been included in the model. Since there is no reaction in the boundary layer, the fluxes on both sides of boundary layer edges are identical. Although not intrinsic to the pore network model, transport through the boundary layer is modeled, at present, using a simple mass transfer coefficient of $2D/d_p$, where d_p is the particle's Sauter mean diameter based on its envelope volume. Across the boundary layer, the fluxes are given by

$$J_{BL} = \frac{2D}{d_p}(C_B - C_L). \tag{16}$$

The matrix equations (11) and (12) must therefore be modified for entries corresponding to boundary layer edges i, to incorporate Eq. (16). Whether the node j corresponds to a surface node or the far-field boundary node, the elements $\overline{\overline{A}}_{neg}(i,j)$ and $\overline{\overline{A}}_{pos}(i,j)$ are set equal to one. Further, for boundary layer edges i, Eqs. (12a) and (12b) are modified as follows:

$$\overline{\overline{\phi}}_{pos}(i,i) = \frac{2}{d_p}. \tag{17a}$$

$$\overline{\overline{\phi}}_{neg}(i,i) = \frac{2}{d_p}. \tag{17b}$$

Finally, to set the sum of fluxes into each node to zero for the nodes that obey this modified version of Kirchoff's current law, the following matrix equation is used,

$$\overline{\overline{A}}_{big}^{T}\begin{bmatrix} \overrightarrow{J^-} \\ \overrightarrow{J^+} \end{bmatrix} = \vec{0} \tag{18}$$

When combined with Eq. (10), this yields a linear system to be solved for the vector of unknown node concentrations, $\vec{C}$,

$$\overline{\overline{A}}_{big}^{T}\left[-D\overline{\overline{\phi}}_{neg}\left(\overline{\overline{A}}\circ\overline{\overline{A}}_{neg}\right) - D\overline{\overline{\phi}}_{pos}\left(\overline{\overline{A}}\circ\overline{\overline{A}}_{pos}\right)\right]\left[\vec{C}\right] = \vec{0} \tag{19}$$

The far-field boundary node concentration is therefore not calculated from the modified Kirchoff's current law since its fluxes do not sum to zero and its value is simply imposed. Similarly, since there is no flux into dead-end nodes, the elements in the rows of Eq. (18) corresponding to the dead-end nodes are all zero (see Table 1), so the dead-end node concentrations are determined from Eqs. (5a) and (6a) using the concentrations of the dead-adjacent nodes.

The pore network model is well-suited for coupling with generalized 1-D effectiveness factor models, which can accurately represent the reaction–diffusion behavior within the irregularly shaped microporous solid, but which require the average concentration [30] on the interface between the microporous solid and the resolved pores (and external surface). To calculate the average concentration on the interface

between resolved pores and microporous solid once the node concentrations have been determined from solving Eq. (19), the average concentration in each pore, $C_{avg,i}$, is first determined from integration of the analytical concentration profiles in Table 1, which, after using hyperbolic identities, yields, for all pore types:

$$C_{avg,i} = \frac{(C_{B,i} + C_{L,i})(\cosh(\phi_i L_i) - 1)}{\phi_i L_i \sinh(\phi_i L_i)} \tag{20}$$

The surface-averaged concentration is then determined for the entire pore network using

$$C_{avg,s} = \frac{\sum_i P_i L_i C_{avg,i}}{\sum_i P_i L_i}. \tag{21}$$

Replacing P_i with A_i yields the volume-averaged concentration, $C_{avg,V}$,

$$C_{avg,V} = \frac{\sum_i A_i L_i C_{avg,i}}{\sum_i A_i L_i}. \tag{22}$$

It is recalled that the pore network model does not account for concentration gradients in the pores' radial direction, so Eqs. (21) and (22) simply represent two different ways of weighting the same $C_{avg,i}$ data; either weighting each pore's contribution by its surface area fraction (Eq. (21)) or by its volume fraction (Eq. (22)).

The average concentration on the interface between the microporous solid and resolved pores (and external surface) is the key quantity to be obtained from the pore network model and can be used with a generalized 1-D effectiveness factor model for the irregularly shaped microporous solid. For a first order reaction, the effectiveness factor for the microporous solid, η, is independent of the interface concentration, and the pore network model and the effectiveness factor model can be solved independently. Nonetheless, the average interface concentration (as well as the average external surface concentration) is still needed to compute the all-important volume-integrated reaction rate, which is given by

$$R_{particle} = \eta R(C_{avg,s+ext}) \tag{23}$$

The volume integrated reaction rate, $R_{particle}$, is the key quantity to be computed by particle-scale submodels in reactor-scale simulations. For nonlinear reaction rate expressions (with approximate or numerical solutions to the reaction–diffusion equation), the pore network model would be coupled to the effectiveness factor model through $C_{avg,s}$ and would need to be solved simultaneously, since the reaction rate, k'', is dependent on η (see Section 3.2), which depends on $C_{avg,s}$ for nonlinear rate forms, which in turn depends on the concentration in the pores via Eq. (21). All computations outlined in this section were performed using MATLAB and require just a couple seconds to run on a desktop computer.

2.5. Pore-resolving CFD simulations for validation

Pore-resolving CFD simulations were performed to validate the automated pore network reaction–diffusion model, using the same biomass char particle geometries that were imaged with micro-CT, processed, and segmented into microporous solid and resolved pores, as described in Section 2.1. For the CFD simulations, a spherical boundary layer was added outside the particle, as shown in the cross-section in Fig. 3(a), and the microporous solid, resolved pores, and external boundary layer regions were all meshed using a free tetrahedral meshing algorithm. Approximately two million elements were used in each particle's mesh, based on mesh convergence studies [18], with the elements being more heavily concentrated in the microporous solid, resolved pores, and boundary layer regions closer to the particle.

As described in Section 1, in the 3-D pore-resolving CFD, conservation equations based on first principles are solved in the resolved pores (and in the external boundary layer), since many of the resolved pores are too large to be treated accurately at the subgrid-scale. In the microporous solid, an effective continuum approach is employed. This is depicted schematically in Fig. 3(b). All heterogeneous reaction occurs within the microporous solid since its unresolved pore surface area is orders of magnitude greater than that of the external surface or resolved pores. Thus, a volumetric reaction rate is employed in the CFD simulations, with Arrhenius rate constant indicated by k'''. Thus, reaction which occurs "on" the external surface or "on" the surface of the resolved pores actually occurs within the subgrid-scale "roughness" (pores) adjacent to those surfaces.

To simulate zone II biomass char particle combustion outside the volatile flame region, far-field boundary conditions for a temperature of $T_\infty = 1373$ K and an oxygen mole fraction of $x_{O_2,\infty} = 0.12$ were imposed on the outside of the spherical domain [52]. CFD simulations were also performed using different far-field boundary temperatures (see Section 3.2). Steady-state simulations were performed, which are sufficient to examine the impact of a given state of the morphology on the interplay of reaction and diffusion. As in previous simulations, all particles were scaled isotropically to have the same effective diameter, so the pore network reaction–diffusion model was also scaled accordingly before performing the calculations detailed in Section 2.4. The CFD simulations were performed using ANSYS Fluent, with each simulations requiring approximately 72–96 h while running on 16 cores. Details of the pore-resolving CFD simulations are available elsewhere [17,18].

2.6. Transport and kinetic parameters and particle temperature

To ensure a valid comparison, all parameters required by the pore network model were chosen to be consistent with the CFD simulations that were used for validation. These parameters include the diffusion

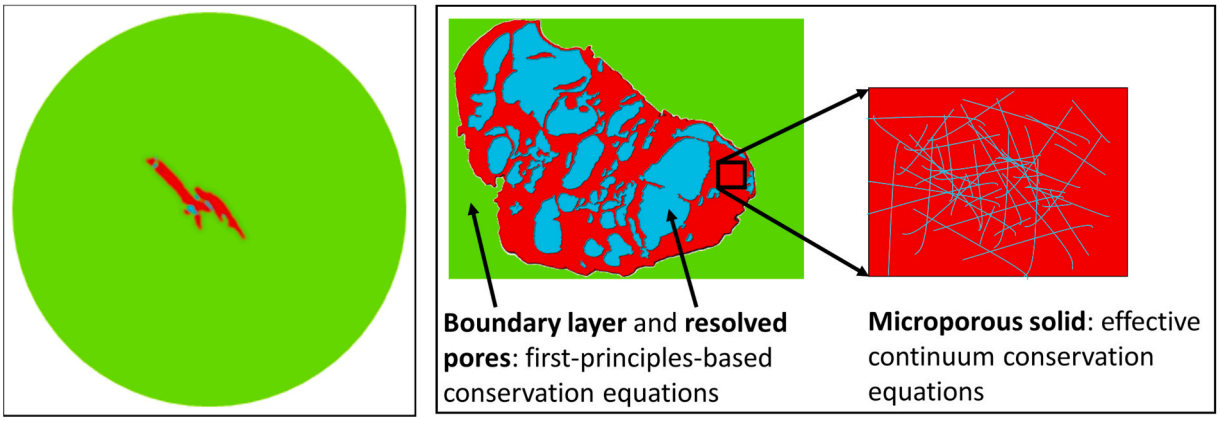

Fig. 3. (a) Cross-section of the simulation domain for 3-D pore-resolving CFD, showing microporous solid (red), resolved pores (blue), and external boundary layer (green). (b) Illustrative depiction of pore-resolving CFD simulation approach by region.

coefficient and temperature, with the latter taken to be the volume-averaged particle temperature from the CFD simulation (but which could be evaluated from a zero-dimensional energy balance in future implementations, or a one-dimensional version to account for non-isothermal particles). The pore network model's reaction rate constant per unit surface area on the resolved pore walls, k'', ([m/s]), is related to the volumetric reaction rate within the microporous solid volume used in CFD, k'''(note the units of k''' are [1/s] = [kmol O_2/m^3/s/(kmol O_2/m^3)]), via

$$k'' = \frac{k'''\eta V_{mps}}{\left(S_{ext} + \sum_i P_i L_i\right)} \tag{24}$$

where the particle's microporous solid volume is V_{mps}, its external surface area is S_{ext}, and the interfacial surface area between the resolved pores and microporous solid is $\sum_i P_i L_i$.

Consistent with the discussion in Section 2.4, the effectiveness factor for the microporous solid, η, is taken from CFD at present, since the current objective is solely to evaluate the pore network model. As discussed in Section 1, in future implementations, η can be obtained from a generalized 1-D effectiveness factor model for the irregular microporous solid, e.g., [24,29], and used in conjunction with the pore network reaction–diffusion model to obtain the overall reaction rate via Eq. (23).

3. Results and discussion

The geometrically faithful pore network reaction–diffusion model proposed in this paper has been tested by comparing the morphological properties of the 1-D pore space obtained by automated morphology measurement and graph generation (Section 2.3) with the 3-D morphological properties obtained from micro-CT and by comparing oxygen mole fraction predictions from the pore network model (Section 2.4) with those obtained from 3-D pore-resolving CFD simulations. Mole fraction distributions are determined from concentrations using the ideal gas equation of state. To verify the numerical implementation of the pore network model, it was confirmed that concentration maxima do not occur within the network, that local maxima do not occur within dead-end segments of the network, and that $\left(J_i^- - J_i^+\right) > 0$ for every edge, i, in the network (since all reactions consume oxygen).

3.1. Pore-space morphology

The 3-D pore space segmented from particle P1 is shown in Fig. 4(a), and the graph network generated for the pore space is shown in Fig. 4 (b). The real pore space exhibits a significant degree of directional porosity, with the longest pores being primarily oriented parallel to the particle's major axis. Many of the pores have high aspect ratios, which is typical of biomass particles [53], and are approximately cylindrical, although the presence of roughness and non-circular cross-sections is noted. The presence of isolated pores and pore clusters can be observed in the 3-D view as well as in the graph representation. While most of the longer pores run parallel to each other and to the particle's major axis, the graph representation indicates the presence of shorter edges connecting the longer pores to each other and to nodes on the particle's external surface, typical of the pore structure of woods derived from tracheid cells and pits [53–55]. Analysis of node connectivity indicated that more than 97% of the nodes were connected to three or fewer pores.

Frequency histograms for pore diameter, pore length, the shortest distance from pore center to the external surface (averaged for paths through the two end nodes), and (post-isotropic scaling) pore Thiele modulus, Φ_i (for $T_\infty = 1373$ K) are shown in Fig. 5 for the three particles examined in this study. For all three particles, at least 98% of pores are below 20 μm in diameter, and the frequency histograms for diameter are right skewed with long tails. In Crowley et al.'s micro-CT study [21], the probability density functions for pore radius (referred to as "pore-to-surface distance" therein) also exhibited a strong right skew, maxima below radii of 5 μm, and very few pores with radii above 10 μm for pyrolyzed oak and fir, which are all similar to the frequency histograms for the pyrolyzed poplar pore diameters in Fig. 5(a), including the small number of pores with diameters above 20 μm. However, the oak sample in Crowley et al. exhibited a biomodal distribution with a second peak at 4.5 μm radius, which is not seen in Fig. 5(a). Figs. 5(b) and (c) show that frequency histograms for pore length and for shortest distance from pore center to the external surface are also right skewed with long tails, and for all three particles, at least 94% of pores are below 20 μm in length, and 95% of pores are within 20 μm of the external surface. Fig. 5(d) shows that pore Thiele moduli are also right skewed, indicating that most pores, individually, have small diffusion limitations and are near kinetic control. The particles have qualitatively similar histograms, although particle P1, being smaller than the others (see Fig. 1), contains fewer pores and thus fewer edges and nodes than the others. The significant skewness of Figs. 5(b) and 5(d) highlights the presence of many shorter pores which individually have minimal diffusion limitations but serve to connect larger pores with each other and with the surface and thus influence reactant transport throughout the pore network.

Since the pore network model aims to predict average concentrations and since the largest pores provide the largest contribution to the volume and area, Fig. 5(e)-(h) shows the volume-weighted frequency histograms corresponding to those in Fig. 5(a)-(d), using the same number of bins. The volume-weighted histograms are noticeably less skewed than the frequency histograms, as in [56], and show less consistent behavior between the particles. Of course, the larger diameter pores and the longer pores contribute an outsized share of the pore volume, as seen in Figs. 5(e) and (f). The shift between Figs. 5(c) and (g) can be explained by noting that the definition of "pore distance" is the shortest distance

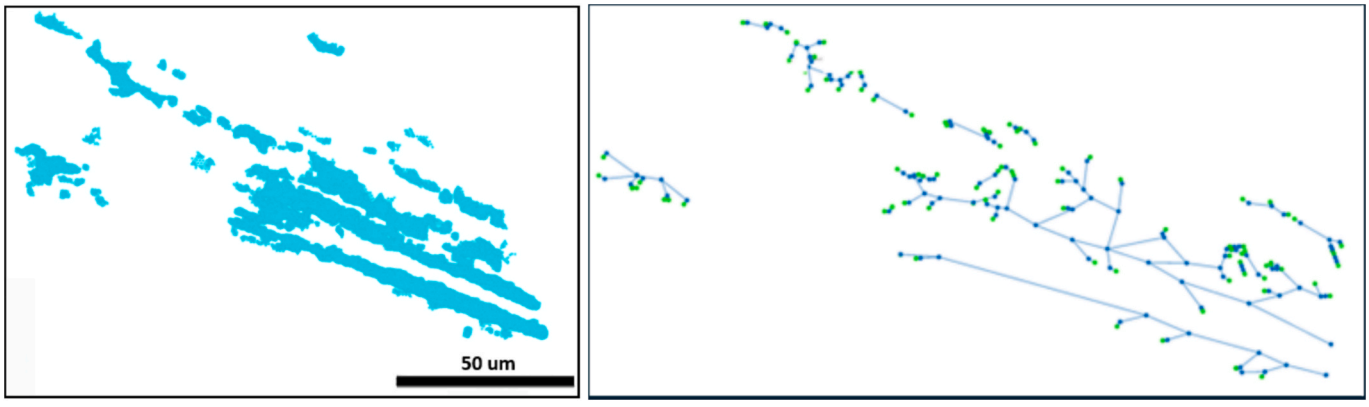

Fig. 4. (a) Three-dimensional pore space of biomass char particle P1, and (b) its graph representation, with edges in blue, interior nodes in blue, and surface nodes in green.

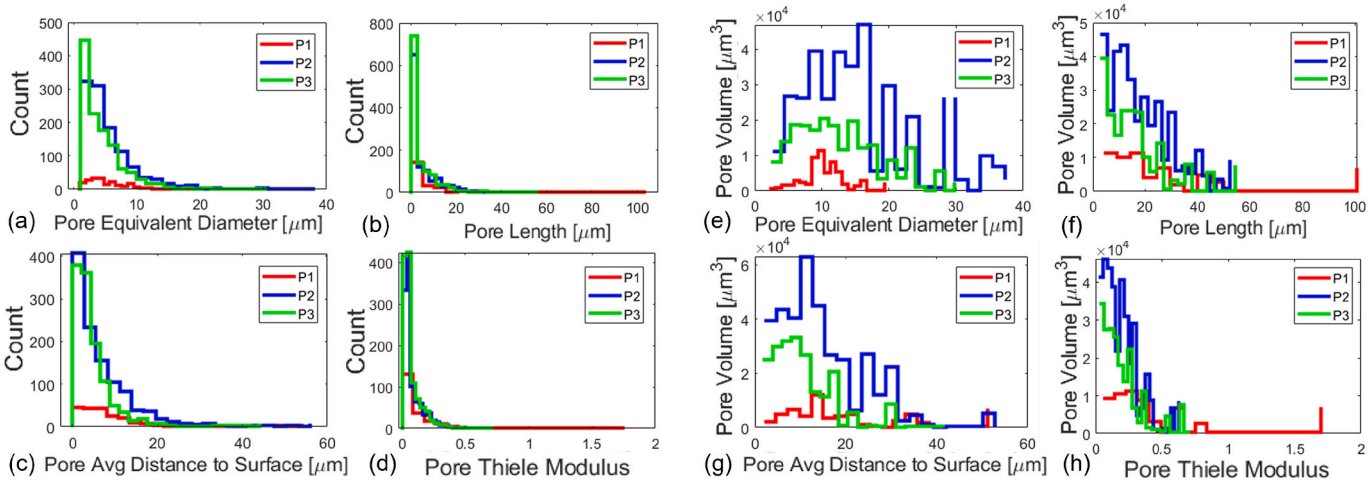

Fig. 5. Frequency histograms for all three particles for (a) pore diameter, (b) pore length, (c) minimum distance from pore center to external surface, and (d) pore Thiele modulus, as well as volume-weighted frequency histograms for (e) pore diameter, (f) pore length, (g) minimum distance from pore center to external surface, and (h) pore Thiele modulus.

Table 2
Total pore volume (V) and surface area (S) for the pore network model and 3-D particles, and relative errors (RE) in pore network model calculations.

Particle	$V_{pore,\ network}$	$V_{pore,3D}$	RE_V	$S_{pore,\ network}$	$S_{pore,3D}$	RE_S
P1	6.02e-14 m^3	6.57e-14 m^3	−8.37%	3.081e-8 m^2	3.121e-8 m^2	−1.28%
P2	3.67e-13 m^3	4.31e-13 m^3	−14.8%	1.644e-7 m^2	1.749e-7 m^2	−6.00%
P3	2.10e-13 m^3	2.61e-13 m^3	−19.5%	1.188e–7 m^2	1.220e–7 m^2	−2.61%

from the pore's center to the external surface, rather than from its ends, giving rise to larger distances for longer, higher-volume pores. The shift toward higher Thiele moduli between Figs. 5(d) and (h) indicates that the large-volume pores experience greater diffusion limitations than the smaller volume pores. Thus, the large-volume pores affect reactant concentration in the network not only through their connectivity, which is predominantly the case with the shorter pores, but also directly via internal diffusion limitations. The pores driving this shift are the longer pores (as opposed to any potential shorter, wider pores).

The total volume and surface area of the 1-D pores calculated by the automated pore network model are compared to the total pore volume and pore surface area of the 3-D pore space from micro-CT simulated in CFD in Table 2. Each pore's volume is determined from the product of its length and average cross-sectional area, while each pore's surface area is determined from the product of its length and average perimeter, obtained as described in Section 2.3. The total pore volumes in the pore network models are underpredicted by between 8% and 19.5% compared to the 3-D pore space, while total pore surface areas are underpredicted by only 1% to 6%. Potential sources of error are associated with the morphological differences between the straight, constant cross-section, 1-D pores in the model and the real 3-D pore space, and with inaccuracies in counting voxels near pore ends, especially near branches.

3.2. Pore network reaction-diffusion model

Pore-resolving CFD results for oxygen mole fraction (x_{O2}) and temperature distributions in and around cross-sections of the three particles are shown in Fig. 6 for $T_\infty = 1373$ K. For zone II conditions, significant variations of oxygen mole fraction occur within the particles, in both the large pores and in the microporous solid regions, with local minima in x_{O2} occurring within microporous solid regions. As observed previously [9,18], the large pores act as conduits for diffusion of oxygen, so the distribution of reactant is non-monotonic with distance from the particles' external surface. This renders effective continuum models inaccurate [9]. As in these previous studies, the temperature distributions in and around the particles are more uniform than the species distributions, due to the small Biot number. While the diffusivity within the microporous solid is much smaller than the diffusivity in the resolved pores, the thermal conductivity in the solid is higher, leading to smaller temperature gradients in the particles.

Fig. 7 compares the x_{O2} distributions on the interface between the resolved pores and microporous solid from the pore-resolving CFD simulations (left column) to the x_{O2} distributions predicted by the pore network model for the three particles, for $T_\infty = 1373$ K. To facilitate the visual comparison, the orientation and location of every edge in the graph was determined, and a cylinder with the same cross-sectional area and length as the corresponding pore was placed around that edge. The concentration profiles along each pore were then obtained from Eqs. (4a), (5a), and (6a) in Table 1 and converted to mole fraction profiles. This yields the spatially resolved x_{O2} distributions predicted by the 1-D pore network model shown in the right column of Fig. 7.

It can be observed in Fig. 7 that the automated pore network model qualitatively reproduces the features from the 3-D pore resolving CFD simulations, including predicting regions of relatively high and low oxygen mole fraction, as well as the impacts of pore connections and external pore openings (surface nodes). This indicates that the connectivity of the pores in the automatically constructed network resembles the connectivity of the true pore space, including capturing the presence (and absence) of key pores connecting pores with each other and with the external surface. The similarity in x_{O2} magnitudes between the pore network model and CFD also indicates that the 1-D reaction–diffusion framework outlined in Section 2.4 accounts for the 3-D transport and reaction with sufficient accuracy.

The pore network model (right panel) is, however, observed to predict higher values of x_{O2} in regions where x_{O2} is the lowest in CFD. This appears most widespread for particle P3 but is also noticeable for the two large pores in particle P1, and in some smaller pores in particle P2. However, it is noted that the CFD panels show distributions of oxygen mole fractions on the *interface* between the resolved pores and microporous solid, which are lower than the values away from the pore walls, whereas the pore network model does not account for variations

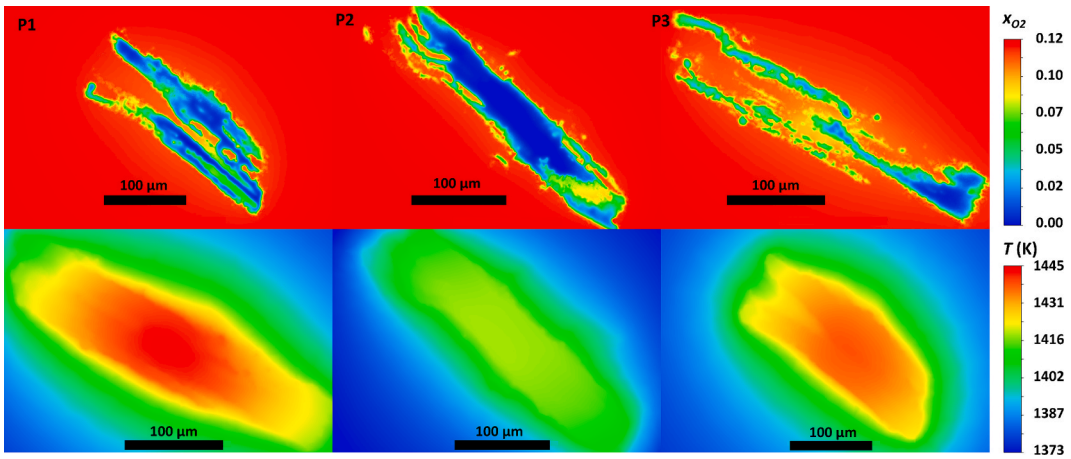

Fig. 6. Oxygen mole fraction (top) and temperature (bottom) distributions in and around cross-sections of the three particles from 3-D CFD, using the same scale for all particles, for $T_\infty = 1373$ K.

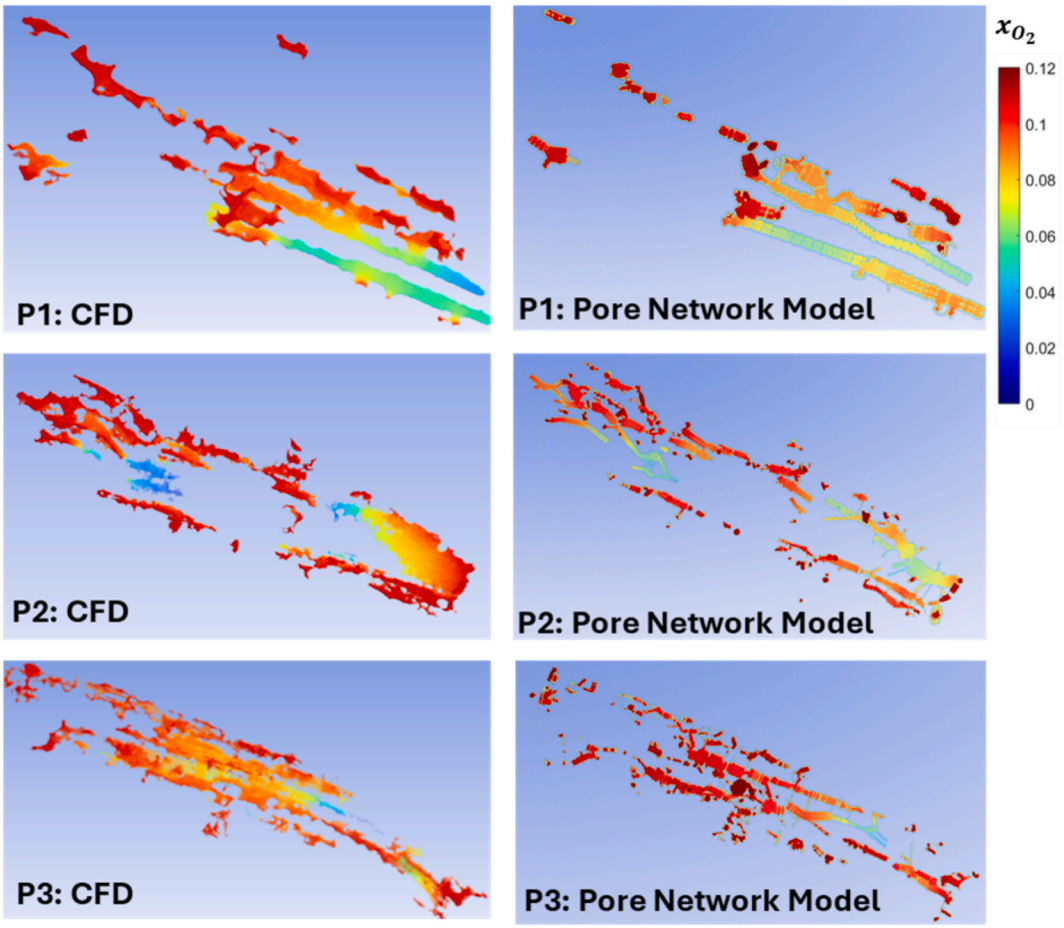

Fig. 7. Oxygen mole fraction distributions in the pore space from 3-D CFD (left), and in the pore network model (right), using the same color map and range, for particles P1 (top row), P2 (middle row), and P3 (bottom row) for $T_\infty = 1373$ K.

in the pores' radial direction. Some overprediction by the pore network model may also be partially due to the conversion from k''' to k'' in Eq. (24), which fails to differentiate between pores according to the amount of surrounding microporous solid. In reality, and in the CFD, reaction occurs within the microporous solid on the surface area of the subgrid-scale, unresolved pores, which is orders of magnitude larger than the external surface area or the surface area of the resolved pores. Therefore, resolved pores which are relatively isolated and surrounded by a greater volume of microporous solid could have a higher flux through their walls (and thus higher k'') than resolved pores that are surrounded by less solid volume. However, the pore network model employs a value of k'' that is identical for every pore.

To facilitate a quantitative comparison, Eq. (21) is used to calculate the surface-averaged concentration on the interface between the microporous solid and resolved pores, since it is the key quantity predicted by the pore network model and must be used with a generalized

Table 3
Surface- and volume-averaged oxygen mole fractions for the pore network model and CFD, and relative errors (RE) for the pore network model predictions, for $T_\infty = 1373$ K.

Particle	$x_{O_2,avg,S}$ Model	$x_{O_2,avg,S}$ CFD	RE $x_{O_2,avg,S}$	$x_{O_2,avg,V}$ Model	$x_{O_2,avg,V}$ CFD	RE $x_{O_2,avg,V}$
P1	0.0900	0.0850	5.88%	0.0871	0.0921	−5.43%
P2	0.0959	0.0933	2.78%	0.0920	0.0991	−7.16%
P3	0.1030	0.0923	11.6%	0.1021	0.0984	3.76%

1-D effectiveness factor model for the irregularly shaped microporous solid to predict $R_{particle}$. Equation (22) is also used to calculate the volume-averaged concentration, since it just represents a different weighting of the $C_{avg,i}$ data. In fact, since the pore network model does not account for radial gradients in pores, its average concentration prediction for each pore from Eq. (20) corresponds more closely, conceptually, to a volume-average than a surface-average. Concentrations are readily converted to mole fractions, $x_{O_2,avg,s}$ and $x_{O_2,avg,V}$, and compared to surface- and volume-averaged mole fractions from CFD, in Table 3, to quantitatively assess the model.

The values of $x_{O_2,avg,s}$ predicted by the pore network model are relatively accurate, with an average relative error of 6.75% for the three particles, which is achieved without any fitting parameters. Similarly, the average magnitude of the relative error for $x_{O_2,avg,V}$ is 5.45%. For the pore network model, which does not account for variations in the radial direction within the pores, there is less difference between $x_{O_2,avg,s}$ and $x_{O_2,avg,V}$, compared to the CFD simulation, as expected. In fact, the pore network model predicts higher values for $x_{O_2,avg,s}$ than $x_{O_2,avg,V}$, which is explained by again noting that the two quantities are just two different ways of weighting the same $C_{avg,i}$ data. The $x_{O_2,avg,s}$ predictions for all three particles are higher than the results from CFD, while two of the three $x_{O_2,avg,V}$ predictions are lower than their respective CFD values. This is consistent with observations from Fig. 7 and is likely due, at least in part, to the pore network model being a 1-D model with concentration variations only in the pores' axial direction, whereas the pore-resolving CFD predicts lower values on the pore walls ($x_{O_2,s}$) and higher values away from the pore walls.

To further evaluate the performance of the pore network model, simulations were also performed for far-field boundary temperatures of 1423 K, 1473 K, and 1523 K, giving rise to increasing levels of diffusion limitations and decreasing effectiveness factors. Fig. 8(a) compares predictions of $x_{O_2,avg,s}$ from the automated pore network reaction–diffusion model to those calculated by the pore resolving CFD simulation as a function of the overall effectiveness factor, $\eta_{overall}$, which is defined using the concentration at the far-field boundary as the reference for defining the ideal reaction rate:

$$\eta_{overall} = \frac{R_{particle}}{R(C_{avg,\infty})} \tag{25}$$

The agreement between the pore network model and the pore resolving simulation is relatively constant across the range of overall effectiveness factors, with slightly increasing relative errors at higher temperatures and lower $\eta_{overall}$ values. As in the preceding results, which were compared in detail for $T_\infty = 1373$ K, the pore network model predictions for $x_{O_2,avg,s}$ are most accurate for particle P2, while those for particle P3 exhibit the greatest degree of overprediction.

Similar to the discussion surrounding Table 3, Fig. 8(a) indicates that the pore network model predictions for $x_{O_2,avg,s}$ slightly exceed the CFD values for all cases, while according to Fig. 8(b), those for $x_{O_2,avg,V}$ fall below CFD values for all cases for two of the three particles. This is likely because the 3-D CFD resolves radial gradients within pores, whereas by nature of the pore network model treating pores as one dimensional, the predicted $C_{avg,i}$ represent concentrations for the entire volume of pore i, rather than concentrations exclusively at the pore wall. Since the pore network model predictions correspond to the entire cross-section of each pore, one might expect greater accuracy in the pore network model's prediction of $x_{O_2,avg,V}$ than $x_{O_2,avg,s}$, but for the 12 cases tested, the agreement with CFD is similar for the two quantities, with an average relative error in $x_{O_2,avg,s}$ of 8.76%, while the average absolute value of the relative error in $x_{O_2,avg,V}$ is 7.64%. It is noted that this agreement was obtained without the use of fitting parameters, since all model parameters are set to be consistent with CFD (Section 2.6), which implies that any error is due to simplifications inherent in the framework of the pore network model.

One reason for the underprediction of $x_{O_2,avg,V}$ observed in Fig. 8(b) and in Table 3 may be that a 1-D model for transport and reaction in a pore inherently predicts a greater level of reaction at the walls than a model with radial gradients, and thus a lower average concentration over a given cross-section (and volume). This is because in a 1-D model, the walls have access to the bulk concentration at any axial location, due to the assumption of infinitely fast radial diffusion. By contrast, the 3-D simulation allows for radial gradients, which lowers the concentration of reactant at the wall, lowering reaction rates and increasing the volume-average concentration in the pore compared to the idealized 1-D model. Another reason for the underprediction of $x_{O_2,avg,V}$ could be due to the automated graph model underpredicting pore volume to a greater extent

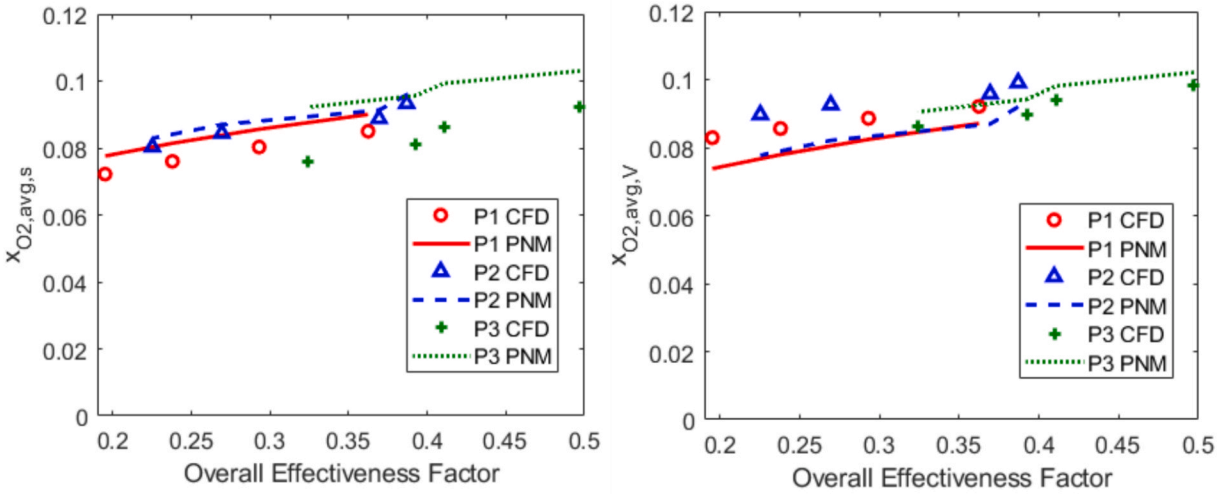

Fig. 8. (a) Surface-averaged oxygen mole fractions for the pore network model and CFD, and (b) volume-averaged oxygen mole fractions for the pore network model and CFD, for four far-field boundary temperatures.

than it underpredicts pore surface area (Table 2). This is indicative of an overprediction of the perimeter per unit area ratio, P/A, in Eq. (1). This increases the reactant sink term in the governing equation, resulting in lower oxygen mole fraction predictions throughout the pore network compared to the CFD. Finally, it is conceivable that diffusion of oxygen through the external surface into the microporous solid may increase its concentration in the resolved pore space in CFD, either directly or indirectly, whereas this is not accounted for in the pore network model.

4. Conclusions

A novel, geometrically faithful pore network model for diffusion and reaction in the pore space of biomass char particles has been proposed, developed, and tested, in which the geometry and connectivity of every pore in a graph network is obtained from automated processing of 3-D micro-CT imaging data. The pore network model employs a 1-D reaction–diffusion equation in each pore, accounting for internal, dead-end, and surface pores, and solves for the concentration at every node in the network by setting the sum of the molar fluxes into every node to zero. The morphological properties of the pore network were compared to those obtained directly from 3-D image analysis, and total pore volumes agreed to within 8% to 19.5% while total pore surface areas agreed to within 1% to 6% for the three particles tested.

The pore network reaction–diffusion model is validated by comparing spatial variations of oxygen mole fractions from the model to those in the 3-D pore space and by comparing surface- and volume-averaged oxygen mole fractions to corresponding results from 3-D, geometrically faithful, pore-resolving CFD simulations of zone II combustion for 12 cases. The geometrically faithful simulations exhibited non-monotonic distributions of oxygen mole fraction with distance from the particle surface due to the large, resolved pores facilitating accelerated transport throughout the particles. For the three particles tested, the pore network model captures regions of high and low oxygen mole fraction and the effects of pore connectivity and external surface openings, indicating that the automated network construction, morphological characterization, and reaction–diffusion framework provides a good representation of the 3-D pore space and the 3-D reaction and transport therein. The model achieved good quantitative agreement with the micro-CT-based CFD simulations without using any fitting parameters, with average relative errors in surface- and volume-averaged oxygen mole fractions of less than 10% for the 12 test cases. Potential sources of the overprediction in surface-averaged oxygen mole fraction and the underprediction of volume-averaged oxygen mole fraction have been identified and can serve as the basis for future improvement in the proposed modeling approach.

The pore network reaction–diffusion model predicts the average concentration on the interface between the resolved pores and the surrounding, irregularly shaped microporous solid, which is a quantity required by generalized 1-D effectiveness factor models. The pore network model is thus well-suited for future pairing with an established, generalized 1-D effectiveness factor model for the microporous solid, which can accurately account for irregularly shaped 3-D geometries in a computationally efficient manner, but which cannot account for the presence of the large pores in biomass since they cannot be treated at the subgrid-scale.

Future improvements to the model could include modeling pore growth and surface recession to account for evolution with conversion, or modeling pore blockage via surface accretion. However, these modifications, which would require solving ordinary differential equations to track the growth/shrinkage of each pore, may be unnecessary since most reaction occurs on the surface of the unresolved microporous solid. Future applications of the model will include other thermochemical processes involving biomass, such as gasification. At present, the geometrically faithful pore network model is formulated for first order reactions, which allow for analytical solutions to the reaction–diffusion equation in each pore and decouples the pore network model solution from the effectiveness factor calculation in the microporous solid. The pore network model is also based on one dimensional pores, so while it is well-suited for biomass, it is unclear whether it is appropriate for other porous solids.

While both the pore-resolving CFD and the pore network model presented in this study require pre-processing steps, the pore-resolving CFD simulations required 72–96 h of wall clock time using 16 cores, whereas the pore network model runs in just a few seconds on a desktop computer after the automated pre-processing steps, making it suitable for incorporation in reactor-scale codes employing distributions of realistic biomass particles.

CRediT authorship contribution statement

Thomas Sheehan: Writing – original draft, Visualization, Validation, Software, Methodology. **Marek Trawicki:** Writing – review & editing, Visualization, Validation. **Simcha Singer:** Writing – review & editing, Writing – original draft, Supervision, Software, Resources, Methodology, Funding acquisition, Conceptualization.

Declaration of competing interest

The authors declare the following financial interests/personal relationships which may be considered as potential competing interests: Simcha Singer reports financial support and travel were provided by National Science Foundation. If there are other authors, they declare that they have no known competing financial interests or personal relationships that could have appeared to influence the work reported in this paper.

Acknowledgements

This material is based upon work supported by the National Science Foundation under Grant No. 2211062. Any opinions, findings, and conclusions or recommendations expressed in this material are those of the authors and do not necessarily reflect the views of the National Science Foundation. A portion of this research was also funded by Marquette University's College of Engineering Summer Undergraduate Research Fellowship. The authors thank April Neander and Prof. Zhe-Xi Luo at the University of Chicago Paleo-CT lab for imaging and Prof. Le Zhou at Marquette University for assistance with torrefaction.

Data availability

Data will be made available on request.

References

[1] Lester E, Avila C, Pang CH, Williams O, Perkins J, Gaddipatti S, Tucker G, Barraza JM, Trujillo-Uribe MP. A proposed biomass char classification system. Fuel 2018;232:845–54. https://doi.org/10.1016/j.fuel.2018.05.153.

[2] Pang CH, Lester E, Wu T. Influence of lignocellulose and plant cell walls on biomass char morphology and combustion reactivity. Biomass Bioenergy 2018;119:480–91. https://doi.org/10.1016/j.biombioe.2018.10.011.

[3] Borrego AG, Garavaglia L, Kalkreuth WD. Characteristics of high heating rate biomass chars prepared under N2 and CO2 atmospheres. Int J Coal Geol 2009;77:409–15. https://doi.org/10.1016/j.coal.2008.06.004.

[4] Panahi A, Vorobiev N, Schiemann M, Tarakcioglu M, Delichatsios M, Levendis YA. Combustion details of raw and torrefied biomass fuel particles with individually-observed size, shape and mass. Combust Flame 2019;207:327–41. https://doi.org/10.1016/j.combustflame.2019.06.009.

[5] Ciesielski PN, Crowley MF, Nimlos MR, Sanders AW, Wiggins GM, Robichaud D, Donohoe BS, Foust TD. Biomass Particle Models with Realistic Morphology and Resolved Microstructure for Simulations of Intraparticle Transport Phenomena. Energy Fuel 2015;29:242–54. https://doi.org/10.1021/ef502204v.

[6] Watanabe H. X-ray Computed Tomography Visualization of the Woody Char Intraparticle Pore Structure and its Role on Anisotropic Evolution during Char Gasification. Energy Fuels 2018;32:4248–54. https://doi.org/10.1021/acs.energyfuels.7b03227.

[7] Tremel A, Spliethoff H. Gasification kinetics during entrained flow gasification - Part III: Modelling and optimisation of entrained flow gasifiers. Fuel 2013;107:170–82. https://doi.org/10.1016/j.fuel.2013.01.062.

[8] Roberts DG, Hodge EM, Harris DJ, Stubington JF. Kinetics of Char Gasification with CO2 under Regime II Conditions: Effects of Temperature, Reactant, and Total pressure. Energy Fuel 2010;24:5300–8. https://doi.org/10.1021/ef100980h.

[9] Liang D, Singer S. Pore-Resolving Simulations of Biomass Char Particle Combustion. Proc Combust Inst 2023;39:3293–302. https://doi.org/10.1016/j.proci.2022.07.098.

[10] Kleinhans U, Halama S, Spliethoff H. The role of gasification reactions during pulverized solid fuel combustion: a detailed char combustion model based on measurements of char structure and kinetics for coal and pre-treated biomass. Combust Flame 2017;184:117–35. https://doi.org/10.1016/j.combustflame.2017.05.033.

[11] Ciesielski PN, Pecha MB, Thornburg NE, Crowley MF, Gao X, Oyedeji O, Sitaraman H, Brunhart-Lupo N. Bridging Scales in Bioenergy and Catalysis: a Review of Mesoscale Modeling applications, Methods, and Future Directions. Energy Fuels 2021;35:14382–440. https://doi.org/10.1021/acs.energyfuels.1c02163.

[12] Auriault J. Upscaling Heterogeneous Media by Asymptotic Expansions. J Eng Mech 2002;128:817–22. https://doi.org/10.1061/(ASCE)0733-9399(2002)128:8(817).

[13] Whitaker S. Diffusion and Dispersion in Porous Media. AIChE J 1967;13:420–7. https://doi.org/10.1002/aic.690130308.

[14] S. Whitaker, The Method of Volume Averaging, 1st Edition, Springer Netherlands, Boston, 1999.

[15] Richter A, Nikrityuk PA, Meyer B. Three-dimensional calculation of a chemically reacting porous particle moving in a hot O2/CO2 atmosphere. Int J Heat Mass Transf 2015;83:244–58. https://doi.org/10.1016/j.ijheatmasstransfer.2014.11.090.

[16] Pecha MB, Garcia-Perez M, Foust TD, Ciesielski PN. Estimation of Heat transfer Coefficients for Biomass Particles by Direct Numerical simulation using Microstructured Particle Models in the Laminar Regime. ACS Sustain Chem Eng 2017;5:1046–53. https://doi.org/10.1021/acssuschemeng.6b02341.

[17] Fong G, Jorgensen S, Singer SL. Pore-Resolving simulation of Char Particle Gasification using Micro-CT. Fuel 2018;224:752–63. https://doi.org/10.1016/j.fuel.2018.03.117.

[18] Liang D, Singer S. Pore-Resolving Simulations to Study the Impacts of Char Morphology on Zone II Combustion and Effectiveness factor Models. Combust Flame 2021;229:111405. https://doi.org/10.1016/j.combustflame.2021.111405.

[19] Liang D. A comprehensive study on the effects of porous char particles on drag coefficients under combustion based on Micro-CT and pore-resolving simulation. Powder Technol 2025;460:121073. https://doi.org/10.1016/j.powtec.2025.121073.

[20] Liang D. Investigating the effects of real morphology and flow orientation on heat transfer in char particles using Micro-CT and CFD simulations. Int Commun Heat Mass Transfer 2025;167:109397. https://doi.org/10.1016/j.icheatmasstransfer.2025.109397.

[21] Crowley MF, Sitaraman H, Klinger J, Usseglio-Viretta F, Thornburg NE, Brunhart-Lupo N, Pecha MB, Dooley JH, Xia Y, Ciesielski PN. Measurement of Transport Properties of Woody Biomass Feedstock Particles before and after Pyrolysis by Numerical Analysis of X-Ray Tomographic Reconstructions. Front Energy Res 2022;10:1–14. https://doi.org/10.3389/fenrg.2022.850630.

[22] Dernbecher A, Bhaskaran S, Vorhauer-Huget N, Seidenbecher J, Gopalkrishna S, Briest L, Dieguez-Alonso A. Investigation on the intra-particle anisotropic transport properties of a beech wood particle during pyrolysis. Particuology 2025;98:172–90. https://doi.org/10.1016/j.partic.2025.01.006.

[23] Buffham BA. Design relations for hollow catalyst pellets. Transactions of the Institution of Chemical Engineers A 2000;78:269–82. https://doi.org/10.1205/026387600527130.

[24] Aris R. A Normalization for the Thiele Modulus. Ind Eng Chem Fundam 1965;4:227–9. https://doi.org/10.1021/i160016a025.

[25] Burghardt A, Kubaczka A. Generalization of the effectiveness factor for any shape of a catalyst pellet. Chem Eng Process 1996;35:65–74. https://doi.org/10.1016/0255-2701(95)04115-X.

[26] Mariani NJ, Keegan SD, Martínez OM, Barreto GF. A one-dimensional equivalent model to evaluate overall reaction rates in catalytic pellets. Chem Eng Res Des 2003;81:1033–42. https://doi.org/10.1205/026387603322482266.

[27] Keegan SD, Mariani NJ, Martínez OM, Barreto GF. Behavior of catalytic pellets at high reaction rates. The effect of edges, Ind Eng Chem Res 2006;45:85–97. https://doi.org/10.1021/ie050740m.

[28] Mocciaro C, Mariani J, Martínez OM, Barreto GF. A Three-Parameter One-Dimensional Model to Predict the Effectiveness factor for an Arbitrary Pellet Shape. Ind Eng Chem Res 2011;50:2746–54. https://doi.org/10.1021/ie101296d.

[29] Mariani NJ, Taulamet MJ, Keegan SD, Martínez OM, Barreto GF. Prediction of effectiveness factor using one-dimensional approximations for complex pellet shapes and abnormal kinetics expressions. Ind Eng Chem Res 2013;52:15321–9. https://doi.org/10.1021/ie4005805.

[30] Keegan SD, Mariani NJ, Martínez OM, Barreto GF. Behaviour of smooth catalysts at high reaction rates. Chem Eng J 2005;110:41–56. https://doi.org/10.1016/j.cej.2005.04.013.

[31] Donaubauer PJ, Hinrichsen O. Evaluation of Effectiveness Factors for Multicomponent Diffusion Models inside 3D Catalyst Shapes. Ind Eng Chem Res 2019;58:110–9. https://doi.org/10.1021/acs.iecr.8b04922.

[32] Yang X, Yu F, Shang H, Li Z, Wang S, Xing Y, Gui X. Comprehensive review of porous particles: Multiscale structure, flow, and transport characteristics. Powder Technol 2025;453:120594. https://doi.org/10.1016/j.powtec.2024.120594.

[33] Fathiganjehlou A, Peters EAJF, Buist KA, Kuipers JAM. Multi-scale Pore Network Modeling of a reactive packed bed. Chem Eng J 2024;496. https://doi.org/10.1016/j.cej.2024.153584.

[34] Claassen CMY, Fathiganjehlou A, Peters EAJF, Buist KA, Baltussen MW, Kuipers JAM. Mechanical Solute Dispersion in slender packed bed reactors: Comparing Pore Network Modeling and Particle-Resolved CFD. Int J Heat Mass Transf 2025;240:126630. https://doi.org/10.1016/j.ijheatmasstransfer.2024.126630.

[35] Yancy-Caballero D, Ling LY, Fujita A, Ferreira JE, Driemeier C. Intraparticle Connectivity in Sugarcane Bagasse unveiled by Pore Network Modeling. Bioenergy Res 2019;12:546–57. https://doi.org/10.1007/s12155-019-09993-6.

[36] Edeh IG, Masek O, Fusseis F. 4D structural changes and pore network model of biomass during pyrolysis. Sci Rep 2023;13. https://doi.org/10.1038/s41598-023-49919-z.

[37] Sadeghi MA, Aghighi M, Barralet J, Gostick JT. Pore network modeling of reaction-diffusion in hierarchical porous particles: the effects of microstructure. Chem Eng J 2017;330:1002–11. https://doi.org/10.1016/j.cej.2017.07.139.

[38] Ye G, Sun Y, Zhou X, Zhu K, Zhou J, Coppens MO. Method for generating pore networks in porous particles of arbitrary shape, and its application to catalytic hydrogenation of benzene. Chem Eng J 2017;329:56–65. https://doi.org/10.1016/j.cej.2017.02.036.

[39] Moghaddam M, Abbassi A, Ghazanfarian J, Jalilian S. Investigation of microstructure effects on performance of hierarchically structured porous catalyst using a novel pore network model. Chem Eng J 2020;388. https://doi.org/10.1016/j.cej.2020.124261.

[40] Huang X, Zhou W, Liu B, Jiang K. Pore network modeling of advection-diffusion-reaction in porous media: the effects of channels. Chem Eng Sci 2023;271. https://doi.org/10.1016/j.ces.2023.118577.

[41] Wang Y, Zhang Q, Liu X, Weng J, Ye G, Zhou X. Probing deactivation by coking in catalyst pellets for dry reforming of methane using a pore network model. Chin J Chem Eng 2023;55:293–303. https://doi.org/10.1016/j.cjche.2022.05.015.

[42] Fathiganjehlou A, Peters EAJF, Buist KA, Kuipers JAM. Pore Network Modeling of Intraparticle Transport Phenomena Accompanied by Chemical Reactions. Ind Eng Chem Res 2024. https://doi.org/10.1021/acs.iecr.4c01727.

[43] Sadeghnejad S, Enzmann F, Kersten M. Digital rock physics, chemistry, and biology: challenges and prospects of pore-scale modelling approach. Appl Geochem 2021;131. https://doi.org/10.1016/j.apgeochem.2021.105028.

[44] Xiong Q, Baychev TG, Jivkov AP. Review of pore network modelling of porous media: Experimental characterisations, network constructions and applications to reactive transport. J Contam Hydrol 2016;192:101–17. https://doi.org/10.1016/j.jconhyd.2016.07.002.

[45] Dashtian H, Bakhshian S, Hajirezaie S, Nicot JP, Hosseini SA. Convection-diffusion-reaction of CO 2 -enriched brine in porous media: a pore-scale study. Comput Geosci 2019;125:19–29. https://doi.org/10.1016/j.cageo.2019.01.009.

[46] Bultreys T, Singh K, Raeini AQ, Ruspini LC, Øren PE, Berg S, Rücker M, Bijeljic B, Blunt MJ. Verifying Pore Network Models of Imbibition in Rocks using Time-Resolved Synchrotron Imaging. Water Resour Res 2020;56. https://doi.org/10.1029/2019WR026587.

[47] Thornburg NE, Pecha MB, Brandner DG, Reed ML, Vermaas JV, Michener WE, Katahira R, Vinzant TB, Foust TD, Donohoe BS, Román-Leshkov Y, Ciesielski PN, Beckham GT. Mesoscale Reaction–Diffusion Phenomena Governing Lignin-first Biomass Fractionation. ChemSusChem 2020;13:4495–509. https://doi.org/10.1002/cssc.202000558.

[48] P. Kollmannsberger, Skeleton3D, (2018). https://github.com/phi-max/skeleton3d-matlab (accessed July 15, 2025).

[49] H. Ezer, Calculate the network graph of a 3D voxel skeleton (2023). https://www.mathworks.com/matlabcentral/fileexchange/135281-calculate-the-network-graph-of-a-3d-voxel-skeleton (accessed July 15, 2025).

[50] Schmidt L. The Engineering of Chemical Reactions. Second: Oxford University Press, New York; 2005.

[51] Strang G. Introduction to Applied Mathematics. Wellesley-Cambridge Press; 1986.

[52] Hjärtstam S, Andersson K, Johnsson F, Leckner B. Combustion characteristics of lignite-fired oxy-fuel flames. Fuel 2009;88:2216–24. https://doi.org/10.1016/j.fuel.2009.05.011.

[53] J.A. Petty, Permeability and Structure of the Wood of Sitka Spruce, Proceedings of the Royal Society of London. Series B 175 (1970) 149–166. Doi: 10.1098/rspb.1970.0016.

[54] Berhanu S, Hervy M, Weiss-Hortala E, Proudhon H, Berger MH, Chesnaud A, Faessel M, King A, Pham Minh D, Villot A, Gérente C, Thorel A, Le Coq L, Nzihou A. Advanced characterization unravels the structure and reactivity of wood-based chars. J Anal Appl Pyrolysis 130 2018:249–55. https://doi.org/10.1016/j.jaap.2018.01.024.

[55] Burridge HC, Wu G, Reynolds T, Shah DU, Johnston R, Scherman OA, Ramage MH, Linden PF. The transport of liquids in softwood: timber as a model porous medium. Sci Rep 2019;9. https://doi.org/10.1038/s41598-019-55811-6.

[56] Hyväluoma J, Kulju S, Hannula M, Wikberg H, Källi A, Rasa K. Quantitative characterization of pore structure of several biochars with 3D imaging. Environ Sci Pollut Res 2018;25:25648–58. https://doi.org/10.1007/s11356-017-8823-x.